Materials Today Bio 32 (2025) 101662

Contents lists available at ScienceDirect

Materials Today Bio

journal homepage: www.journals.elsevier.com/materials-today-bio

W-GA nanodots with multienzyme activities alleviate the inflammatory microenvironment in the treatment of acute wounds

Yang Zheng [a,1], Qingrong Li [b,1], Xu Jin [c,1], Mengmei Zhu [b], Qian Liang [a], Yingjie Wu [a], Fuqiang Pan [a], Houhuang Qiu [a], Xianwen Wang [b,*], Decheng Lu [a,**], Huiqiao Huang [a,***]

[a] Research Center of Nanomedicine Technology, The Second Affiliated Hospital of Guangxi Medical University, Nanning, 530000, PR China
[b] School of Biomedical Engineering, Anhui Medical University, Hefei, 230032, PR China
[c] Department of Burns, The First Affiliated Hospital of Anhui Medical University, Hefei, 230022, PR China

ARTICLE INFO

Keywords:
W-GA nanodots
Nanozymes
Multienzyme activities
Acute wounds

ABSTRACT

Acute wounds present a significant clinical challenge due to delayed healing, which is often exacerbated by elevated levels of reactive oxygen species (ROS). These high ROS concentrations hinder the natural healing process, leading to prolonged recovery and increased risk of complications. W-GA nanodots, synthesized via a simple coordination method, have emerged as promising solutions, demonstrating multifunctional enzymatic activity that effectively scavenges ROS. To explore the underlying mechanisms of ROS-induced oxidative stress, we conducted RNA sequencing on macrophages exposed to H_2O_2. The results revealed significant regulation of key stress response pathways, including substantial upregulation of the “p53 signaling pathway” and the “HIF-1 signaling pathway,” both of which are essential for cellular adaptation to oxidative stress. By alleviating oxidative stress, W-GA nanodots not only accelerate wound repair but also improve overall healing outcomes. Notably, RNA sequencing of animal tissue samples revealed that W-GA nanodots activate the “Wnt signaling pathway,” further promoting wound healing. These findings underscore the potential of W-GA nanodots as a novel therapeutic strategy for enhancing wound healing and treating oxidative stress-related conditions, positioning them as promising candidates for future clinical applications in wound care and inflammatory diseases.

1. Introduction

Wound healing is a complex and dynamic process essential for maintaining the integrity and function of the skin and underlying tissues. As a vital protective barrier, effective skin healing plays a crucial role in preventing infections and maintaining internal homeostasis. Wounds are generally classified as acute or chronic, each presenting unique challenges to clinical management. Acute wounds typically progress through well-defined stages of inflammation, proliferation, and remodeling. In contrast to chronic wounds, which often remain stable in the inflammatory phase, acute wounds usually heal within a predictable timeframe, provided that there are no complications [1–3]. However, the healing of acute wounds can be delayed by various factors, particularly elevated levels of reactive oxygen species (ROS) in the wound microenvironment. Excessive ROS accumulation can disrupt normal healing by promoting persistent inflammation, impairing immune function, and hindering key processes such as collagen synthesis, neovascularization, and re-epithelialization [4–6]. Thus, managing ROS levels is a critical strategy for optimizing acute wound healing. Current therapeutic approaches for acute wound treatment focus on reducing inflammation, enhancing tissue regeneration, and preventing infection through methods such as antimicrobial agents, growth factors, and advanced wound dressings [7–10]. Despite these advances, novel strategies that more effectively address the oxidative stress and inflammatory components of wound healing are needed (see Scheme 1).

Nanozymes are artificial enzymes based on nanomaterials with the potential to mimic the catalytic functions of natural enzymes. They offer advantages such as low cost, ease of synthesis, high stability, and tunable activity. As promising medical tools, nanozymes have garnered significant attention and were recognized as one of the top ten emerging

---

[*] Corresponding author.
[**] Corresponding author.
[***] Corresponding author.

E-mail addresses: xianwenwang@ahmu.edu.cn (X. Wang), ludecheng@gxmu.edu.cn (D. Lu), hhq@sr.gxmu.edu.cn (H. Huang).

[1] These authors contributed equally to this work.

https://doi.org/10.1016/j.mtbio.2025.101662
Received 14 January 2025; Received in revised form 28 February 2025; Accepted 13 March 2025

technologies in chemistry for 2022 by the International Union of Pure and Applied Chemistry (IUPAC) [11–13]. Among various nanozymes, those capable of in situ catalysis of the generation of ROS, such as oxidases and peroxidases, have been widely applied in the development of antitumor drugs and novel nanomicrobial agents [14–16]. In contrast, nanozymes with ROS scavenging capabilities, including superoxide dismutase (SOD), catalase (CAT), and glutathione peroxidase (GPx), can mimic the cellular antioxidant defense system to remove ROS and have demonstrated promising therapeutic effects in diseases such as inflammatory bowel disease (IBD), acute liver injury (AILI), and wound healing [17–19]. Consequently, the use of nanozymes to modulate enzymatic activity in the chronic wound microenvironment holds promise for restoring wound immunity and redox balance. For example, the Janus lipase developed by Tingting Wei and colleagues effectively scavenges ROS, restoring tissue redox and immune homeostasis [20–23]. Additionally, the 2 TT-mC6B@$Cu_{5.4}O$ NPs developed by Wentao Wang and colleagues exhibit excellent ROS scavenging and oxygen generation capabilities, which can synergistically alleviate inflammation, improve hypoxic conditions, and promote deep penetration into chronic wound tissues [24]. These methods have the potential to become important strategies for enhancing acute wound healing.

This study reports the synthesis of W-GA nanodots via a simple coordination method involving tungsten and gallic acid (GA). These nanodots exhibit a range of enzymatic activities, including superoxide dismutase (SOD), ABTS radical scavenging, and DPPH radical scavenging activities, and have shown promising results in the treatment of inflammatory bowel disease (IBD) [25]. Given their superior ROS scavenging capabilities, we explored the potential application of W-GA nanodots for acute wound therapy. By modulating the ROS balance and restoring redox and immune homeostasis, these nanodots facilitate wound healing. The synthesis of W-GA nanodots is straightforward: tungsten is cross-linked in a high-molecular-weight PVP network, followed by the addition of gallic acid to the mixture, leading to self-assembly of the W-GA nanodots. High-molecular-weight PVP not only ensures good biocompatibility but also allows for the effective cross-linking of nanozymes, reducing toxicity [26,27]. Additionally, gallic acid, as a natural product, coordinates with tungsten, endowing nanozymes with exceptional antioxidant properties [28]. Systematic characterization confirmed the ability of W-GA nanodots to scavenge ROS, protect cells, and improve the inflammatory microenvironment, ultimately leading to effective chronic wound healing. In diabetic chronic wound animal models, W-GA nanodots significantly accelerated wound healing. Furthermore, skin tissue sequencing revealed that W-GA nanodots effectively activated wound repair pathways in the skin, promoting fibroblast-to-myofibroblast differentiation, collagen synthesis, and angiogenesis. Our study, which combines in vivo and biochemical analyses, represents a significant advancement in addressing the complex challenges of chronic wound healing and offers an effective and adaptable solution for improving patient outcomes.

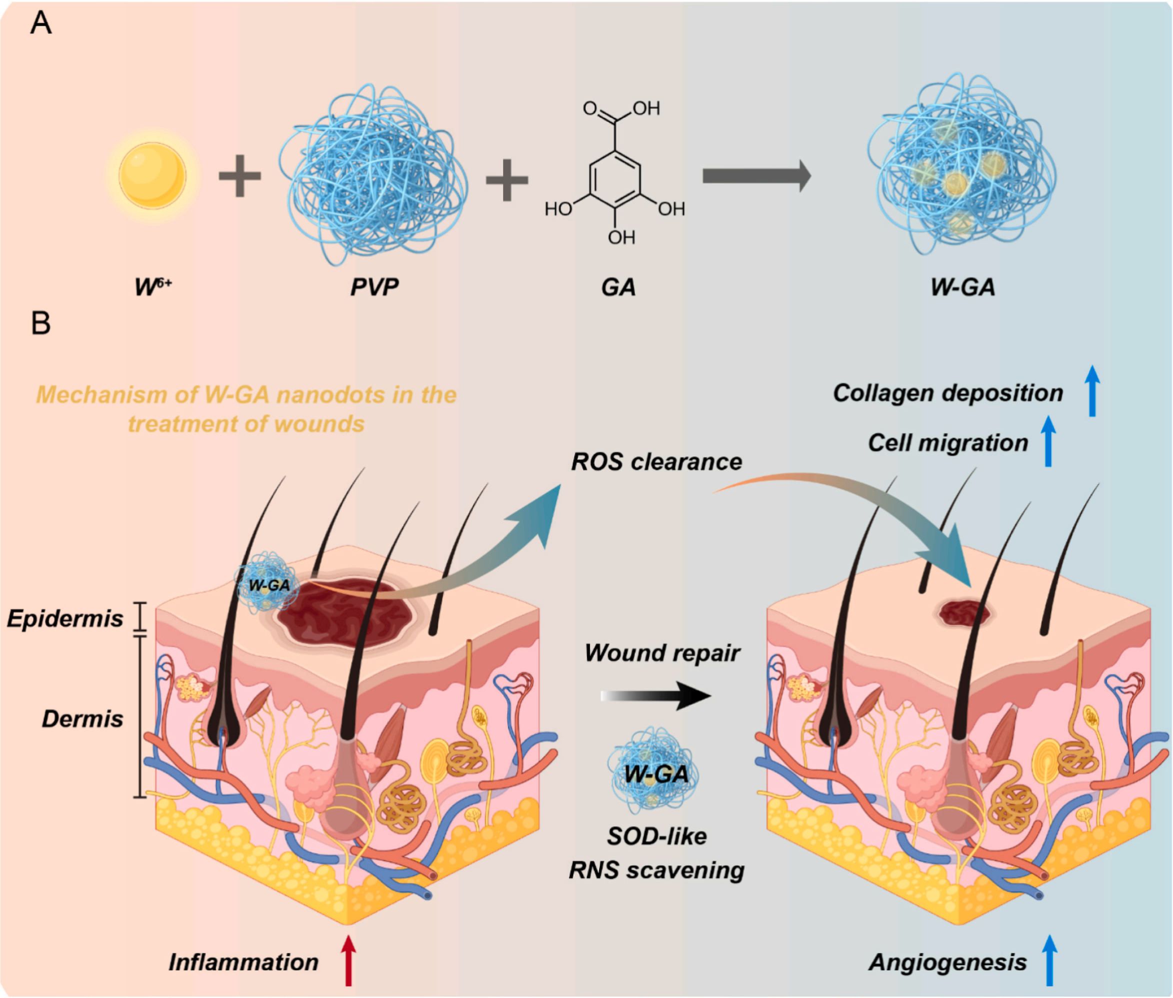

Scheme 1. W-GA nanodots facilitate wound healing via reactive oxygen species (ROS) clearance. A) Synthesis pathway of W-GA nanodots. **B)** These nanodots exhibit superoxide dismutase (SOD) mimetic activity, effectively neutralizing reactive oxygen species (ROS) and reactive nitrogen species (RNS). Their therapeutic action promotes wound healing through enhanced angiogenesis, cellular migration, and collagen deposition.

2. Experimental Section

2.1. Materials

All chemicals were obtained from Sigma–Aldrich and used without further purification unless otherwise specified. The assay kits for 3-amino,4-aminomethyl-2′,7′-difluororesceindiacetate (DAF-FM DA) and 2′,7′-dichlorofluorescein diacetate (DCFH-DA) were obtained from Beyotime Institute of Biotechnology (Shanghai, China). Methylene blue (MB), 2,2′-azinobis (3-ethylbenzothiazoline 6-sulfonate) (ABTS) and 2,2-diphenyl-1-picrylhydrazyl (DPPH) were used. All the water used was purified via a Milli–Q Gradient System.

2.2. Characterization

The absorption spectra in the UV–visible range were measured via a Thermo Scientific Genesys 50 spectrophotometer (China). The optical density (OD) was measured with a universal microplate spectrophotometer (Synergy2 SLFPTAD, USA). X-ray diffraction patterns were obtained via a Rigaku SmartLab SE X-ray diffractometer from Japan. The sample morphology was studied via a transmission electron microscope (JEM-1400 Plus) from Japan. Fluorescence images were acquired via an Olympus Corporation's U-LH100HGAPO fluorescence microscope.

2.3. Synthesis of W-GA nanodots

The W-GA nanodots were synthesized through a modified coordination-driven self-assembly protocol adapted from established methodologies [29]. Initially, 80 mg of tungsten(VI) chloride (WCl_6, 99.9 % purity) was dissolved in 16 mL of ultrapure water under vigorous magnetic stirring (800 rpm) at ambient temperature (25 ± 1 °C) until complete dissolution. Subsequently, polyvinylpyrrolidone (PVP, Mw ≈ 40,000) was introduced as a stabilizer through the addition of an aqueous solution (66 mg/mL, 2 mL), followed by continuous stirring for 60 min to facilitate ligand coordination. A controlled nucleation process was initiated by dropwise infusion (0.25 mL/min) of 2 mL of gallic acid aqueous solution (10 mg/mL) via a peristaltic pump, with a subsequent hydrothermal reaction maintained for 12 h under a N_2 atmosphere to prevent oxidation. Postsynthesis purification employs diafiltration through a regenerated cellulose dialysis membrane against deionized water with complete solvent exchange every 4 h. The resulting colloidal suspension is concentrated via tangential flow filtration and subjected to comprehensive characterization: 1) elemental quantification via inductively coupled plasma optical emission spectroscopy; 2) size distribution analysis via dynamic light scattering; and 3) morphological validation through high-resolution transmission electron microscopy. The final product was stored at 4 °C in nitrogen-filled amber vials to ensure oxidative stability (Supporting Information, Figure S2-4, Table S1).

2.4. In vitro ability of W-GA nanodots to relieve oxidative stress

In vitro experiments were conducted to evaluate the ability of W-GA nanodots to respond to oxidative stress by measuring their ability to scavenge ROS. The scavenging efficiency of W-GA nanodots for nitrogen free radicals was determined via a previously established experimental method for measuring the scavenging effect of ABTS• and DPPH• [30]. To measure the scavenging effect on hydroxyl radicals, which are a type of oxygen free radical, W-GA nanodots of varying concentrations were mixed with Fenton reagent. The resulting solution was then reacted with methylene blue (MB), which fades in the presence of hydroxyl radicals generated by the Fenton reaction. The absorbance of the solution was measured to determine the hydroxyl radical scavenging efficiency of the W-GA nanodots. The scavenging efficiency of W-GA nanodots for another type of oxygen free radical, superoxide anion ($O_2^{\bullet -}$), was evaluated via an SOD enzyme kit.

2.5. Cell culture and cell experiments

L929 cells and RAW 264.7 cells were cultured in DMEM supplemented with 10 % fetal bovine serum, 100 μg/mL streptomycin, and 100 U/mL penicillin in a 5 % CO_2 incubator at 37 °C for subsequent experiments. Cell viability was assessed via a standard CCK8 assay kit after treatment with various concentrations of W-GA nanodots (at a maximum concentration of 200 μg/mL) for 24 h in both cell lines. In addition, L929 cells were stained with calcein-AM/PI after exposure to W-GA nanodots alone or in combination with H_2O_2 to induce oxidative stress. Fluorescence microscopy was used to observe the cells. Furthermore, flow cytometry was performed on RAW 264.7 cells subjected to oxidative stress induced by LPS (1 μg/mL) after staining with DCFH-DA. To observe ROS at the cellular level, L929 cells were incubated with W-GA nanodots for 2 h, washed three times with PBS, and treated with H_2O_2 (500 μM) for 2 h, followed by staining with DCFH-DA or DAF-FM DA. Finally, the ability of W-GA nanodots to remove ROS was evaluated via confocal laser scanning microscopy (CLSM).

2.6. Wound healing

All animal experiments were conducted in strict compliance with the ethical guidelines approved by the Institutional Animal Care and Use Committee of Anhui Medical University (Approval No. LLSC20220731).

Fifteen adult male BALB/c mice (8 weeks old, 22–25 g) were acclimatized for 7 days in a controlled SPF environment (12-h light/dark cycle, 25 ± 1 °C, 60 % humidity). The mice were randomly divided into three experimental groups ($n = 5$ per group): (1) negative control (PBS vehicle, 0.1 mL/day), (2) GA treatment (10 mg/kg/day in PBS), and (3) W-GA nanocomposite (10 mg/kg/day in PBS). Dorsal hair was removed using electric clippers followed by depilatory cream, and general anesthesia was induced via intraperitoneal injection of sodium pentobarbital (50 mg/kg). A full-thickness excisional wound (7 mm diameter, 38.5 mm^2 surface area) was created using sterile surgical scissors.

Topical treatments were administered twice daily using sterile cotton swabs until complete epithelialization. Wound healing progress was quantitatively monitored through daily orthogonal photography under standardized lighting conditions. The major (d_1) and minor (d_2) axes of the wounds (where $d_1 \geq d_2$) were measured using ImageJ software (v1.53), and the wound area (S) was calculated using the elliptical approximation formula:

$$S = (\pi \times d_1 \times d_2) / 4$$

At predetermined time points (Days 4 and 8 postinjury), mice were euthanized via cervical dislocation under deep anesthesia. Tissue samples were collected for further analysis, including wound bed biopsies fixed in 4 % paraformaldehyde for histological examination (H&E and Masson's trichrome staining).

2.7. RNA extraction and quality assessment

Total RNA quality was assessed as follows: concentration and purity were measured via a NanoDrop spectrophotometer < Thermo Scientific NanoDrop 2000 (Thermo Scientific, Waltham, Massachusetts, USA), whereas RNA integrity was evaluated via agarose gel electrophoresis specifically designed for RNA or via the Agilent 2100 Bioanalyzer < Agilent 2100 Bioanalyzer, RNA 6000 Nano Kit 5067-1511 (Agilent Technologies Inc., California, USA).

2.8. Library construction and quality control

A total RNA amount of ≥1 μg was selected for library construction via the NEBNext Ultra II RNA Library Prep Kit for Illumina (New England Biolabs Inc.; Ipswich, Massachusetts, USA) with the NEBNext Ultra Directional RNA Library Prep Kit for Illumina, which is strand specific. mRNAs with polyA tails were enriched via oligo(dT) magnetic beads and then fragmented into smaller pieces via divalent cations at elevated temperatures. The fragmented mRNA was then used as a template to synthesize cDNA with random hexamer primers. The resulting double-stranded cDNA was purified, followed by end repair, the addition of an "A" base at the 3′ end, and the ligation of sequencing adapters. AMPure XP beads were used to select cDNA fragments approximately 400–500 bp in size, which were then amplified via PCR. The PCR products were subsequently purified via AMPure XP beads to generate the final library. The quality of the library was assessed via an Agilent 2100 Bioanalyzer (Agilent Technologies Inc., California, USA) with an Agilent High Sensitivity DNA Kit (Agilent Technologies Inc., California, USA, 5067-4626). The total concentration of the library was measured via PicoGreen (Quantifluor-ST fluorometer, Promega, Madison, Wisconsin, USA, E6090; Quant-iT PicoGreen dsDNA Assay Kit, Invitrogen, California, USA, P7589), and the effective concentration was quantified via qPCR (StepOnePlus Real-Time PCR Systems, Thermo Scientific, Waltham, Massachusetts, USA). Multiplexed DNA libraries were normalized and then pooled in equal volumes. The pooled libraries were diluted, quantified, and sequenced on an Illumina platform in PE150 mode. Read counts mapped to each gene were calculated via HTSeq (v0.9.1) as a measure of the gene's raw expression level. To ensure the comparability of gene expression levels across different genes and samples, expression values were normalized via fragments per kilobase of transcript per million mapped reads (FPKM) values. For

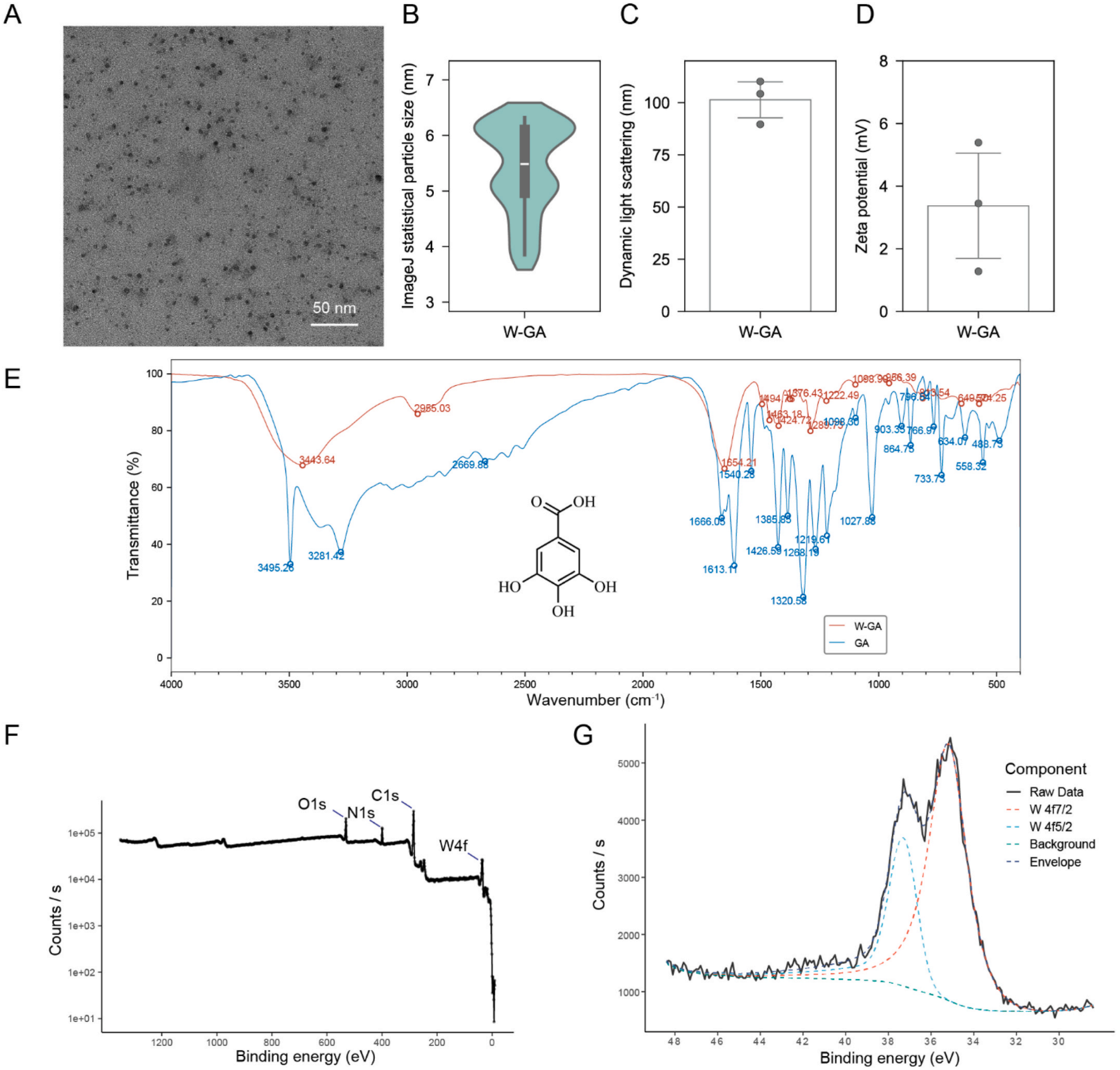

Fig. 1. Synthesis and characterization of W-GA nanodots with multiple enzyme activities. A) TEM images revealing the dot-like structure of W-GA nanodots. Scale bar, 50 nm. B) Statistical analysis of the TEM images was performed via ImageJ. C) The size distribution of the nanodots was measured via dynamic light scattering (DLS). D) The zeta potential of the nanodots was measured. E) FT-IR spectra of W-GA nanodots. F) XPS spectra of the nanodots. G) Core-level spectra of W 4f orbitals in nanodots.

paired-end sequencing, FPKM accounts for fragments where both reads align to the same transcript. Differential expression analysis between two comparison groups was performed via DESeq (v1.38.3). Genes with a $|\log2FoldChange| > 1$ and a P value < 0.05 were considered differentially expressed. GO enrichment analysis was conducted via topGO (v2.50.0), which calculates P values via hypergeometric distribution to identify significantly enriched GO terms (with a significance threshold of P value < 0.05) among the DEGs (all/up/down), thereby determining the main biological functions of the DEGs. KEGG pathway enrichment analysis was performed via clusterProfiler (v4.6.0), with a focus on pathways with P values < 0.05 indicating significant enrichment. Gene set enrichment analysis (GSEA, v4.1.0) was also conducted, which does not require a predefined threshold for differential genes; instead, it ranks all genes on the basis of their differential expression between the two sample groups and tests whether predefined gene sets are significantly enriched at the top or bottom of the ranked list.

2.9. Statistical analysis

Each condition was tested three times independently unless otherwise stated.

3. Results and discussion

Tungsten–gallic acid (W-GA) nanodots were synthesized via a one-pot method and characterized via transmission electron microscopy (TEM). Upon exposure to sunlight, it manifests as a brown liquid (Supporting Information, Fig. S1). Uniformly distributed small black dots were revealed across the field of view in the TEM images, and their size was measured via ImageJ software. The W-GA nanodots had an average diameter of approximately 5.39 ± 0.86 nm (Fig. 1A–B). These black dots are likely representative of the nanozyme active sites. However, dynamic light scattering (DLS) measurements revealed that the W-GA nanodots were approximately 94.7 nm in size in solution (Fig. 1C). This discrepancy was likely due to differences in the behavior of the polymer PVP under solid and solution conditions, as well as the differing principles of the two characterization techniques: the former relies on electron transmission through the material, whereas the latter measures the intensity of light transmission through the solution [31,32]. Additionally, as shown in Fig. 1D, the zeta potential of the W-GA nanodots was measured to be approximately 3.37 ± 2.06 mV. Changes in the characteristic functional groups of W-GA nanodots compared with those of gallic acid were revealed by Fourier transform infrared (FTIR) spectroscopy. Empty orbitals are provided by tungsten as a transition metal ion, whereas lone pairs of electrons are offered by the carboxyl and phenolic hydroxyl groups in gallic acid, leading to the formation of coordination bonds [33,34]. The disappearance of the free carboxylic C=O stretch ($\sim$1748 cm^{-1}) in GA and the emergence of a strong antisymmetric COO^- vibration at 1654.21 cm^{-1} ($\Delta\nu = -93.79$ cm^{-1}) confirmed bidentate binding of the deprotonated carboxyl group to W, forming stable O—W—O bridges. Concurrently, the broad O–H stretching band of GA at 3495.26 cm^{-1} shifts to 3443.64 cm^{-1} ($\Delta\nu = -51.62$ cm^{-1}) with significant broadening, indicative of μ_3-O–W bridging by deprotonated phenolic groups. The exclusive presence of a W–O bending mode at 574.25 cm^{-1} (transmittance: 89.45 %) in the W-GA directly verifies the octahedral WO_6 coordination geometry. This multidentate interaction enhances structural rigidity through π-electron conjugation, as evidenced by attenuated C–O–C and C–H vibrational shifts (1098.30–1222.49 cm^{-1}), suggesting potential applications in designing thermally stable metal–phenolic networks for catalytic and supramolecular systems (Fig. 1E). The presence of tungsten in the nanodots was further confirmed by X-ray photoelectron spectroscopy (XPS) (Fig. 1F). XPS analysis revealed that the spectra could be fitted with the W 4f7/2 and W 4f5/2 characteristic peaks of W^{6+}, indicating that tungsten predominantly exists in the W^{6+} ionic form within the W-GA nanodots (Fig. 1G). The successful synthesis of W-GA nanodots and their assembly into nanostructures via coordination bonding were confirmed by these findings.

Reactive oxygen species (ROS), including hydrogen peroxide (H_2O_2), superoxide anion (O_2^-), singlet oxygen ($^1O_2$), and hydroxyl radicals (·OH), play crucial roles in biological systems [35–37]. In the microenvironment of chronic wounds, complex pathophysiological conditions, potential bacterial infections, cytokine deficiency, and elevated levels of ROS hinder timely wound healing [38]. Clinically, treatments typically involve the use of antibiotics, wound debridement, artificial dermis, and the supplementation of growth factors [39,40]. In the field of nanozyme research, nanozymes with multienzyme activities have been widely applied in wound healing therapies [41]. Therefore, this study evaluated the multienzyme activities of W-GA nanodots through in vitro free radical scavenging assays. A schematic representation of the W-GA nanodot synthesis process is shown in Fig. 2A. Although WCl_6 has limited solubility in water, it was successfully dissolved under vigorous stirring, followed by the addition of an aqueous PVP solution to stabilize the mixture. Finally, 1 mL of a 10 mg/mL gallic acid solution was introduced, resulting in the formation of a brown colloidal solution. The mixture was then dialyzed using a molecular weight cutoff of 8000–14, 000 Da to yield purified W-GA nanodots. The ability of W-GA nanodots to scavenge hydroxyl radicals was assessed via the methylene blue discoloration method (Fig. 2B). At a concentration of 100 μg/mL, the nanodots achieved an impressive hydroxyl radical scavenging efficiency of 93.67 ± 0.77 %, as demonstrated by the observed color changes in methylene blue (Fig. 2C). This finding indicates a strong capacity for neutralizing the oxidative damage caused by hydroxyl radicals. To further explore their antioxidant properties, the scavenging activity of nitrogen radicals was evaluated via ABTS and DPPH assays (F**ig. 2D-E)**. At a concentration of 40 μg/mL, the ABTS scavenging efficiency was 93.83 ± 2.2 %, while the DPPH radical scavenging efficiency reached 62.19 ± 2.44 % at 60 μg/mL. These results are summarized in a mechanistic diagram depicting the pathways for ABTS and DPPH radical scavenging (Fig. 2F), demonstrating the nanodots' ability to neutralize nitrogen radicals through multiple mechanisms. Moreover, W-GA nanodots exhibited enzyme-like activity when tested via a superoxide dismutase (SOD) enzyme assay (Fig. 2G). At a concentration of 200 μg/mL, the nanodots demonstrated an enzyme-mimicking activity of 73.46 ± 6.83 %, further supporting their potential in mitigating oxidative stress by scavenging reactive oxygen species (ROS).

In summary, the results from these assays confirmed that W-GA nanodots possess strong in vitro ROS scavenging capabilities, targeting both hydroxyl and nitrogen radicals while displaying significant enzyme-like activity. These findings position W-GA nanodots as promising agents for counteracting oxidative stress, which plays a crucial role in numerous pathological conditions, including impaired wound healing.

In in vitro enzyme-like activity validation experiments, W-GA nanodots demonstrated multiple enzyme-like activities, effectively scavenging various free radicals. To further investigate their ability to scavenge ROS at the cellular level, W-GA nanodots were used in cell experiments. As shown in Fig. 3A, L929 cells were incubated with W-GA nanodots at concentrations ranging from 0 to 200 μg/mL for 24 h, and cell viability was subsequently assessed. The results indicated that even at the highest concentration of 200 μg/mL, the cell viability remained high at 94.3 ± 1.08 %, suggesting excellent biocompatibility of the nanodots across the tested concentration range. In the presence of oxidative stress, the protective effects of W-GA nanodots became more apparent (Fig. 3B). The viability of the cells treated with 500 μM hydrogen peroxide alone was significantly lower (50.38 ± 1.47 %). However, coincubation with W-GA nanodots at increasing concentrations significantly rescued cell viability, resulting in full recovery (100.56 ± 8.83 %) at a concentration of 100 μg/mL. These findings highlight the potent protective role of W-GA nanodots in neutralizing the harmful effects of ROS.

During early apoptosis, phosphatidylserine translocates from the

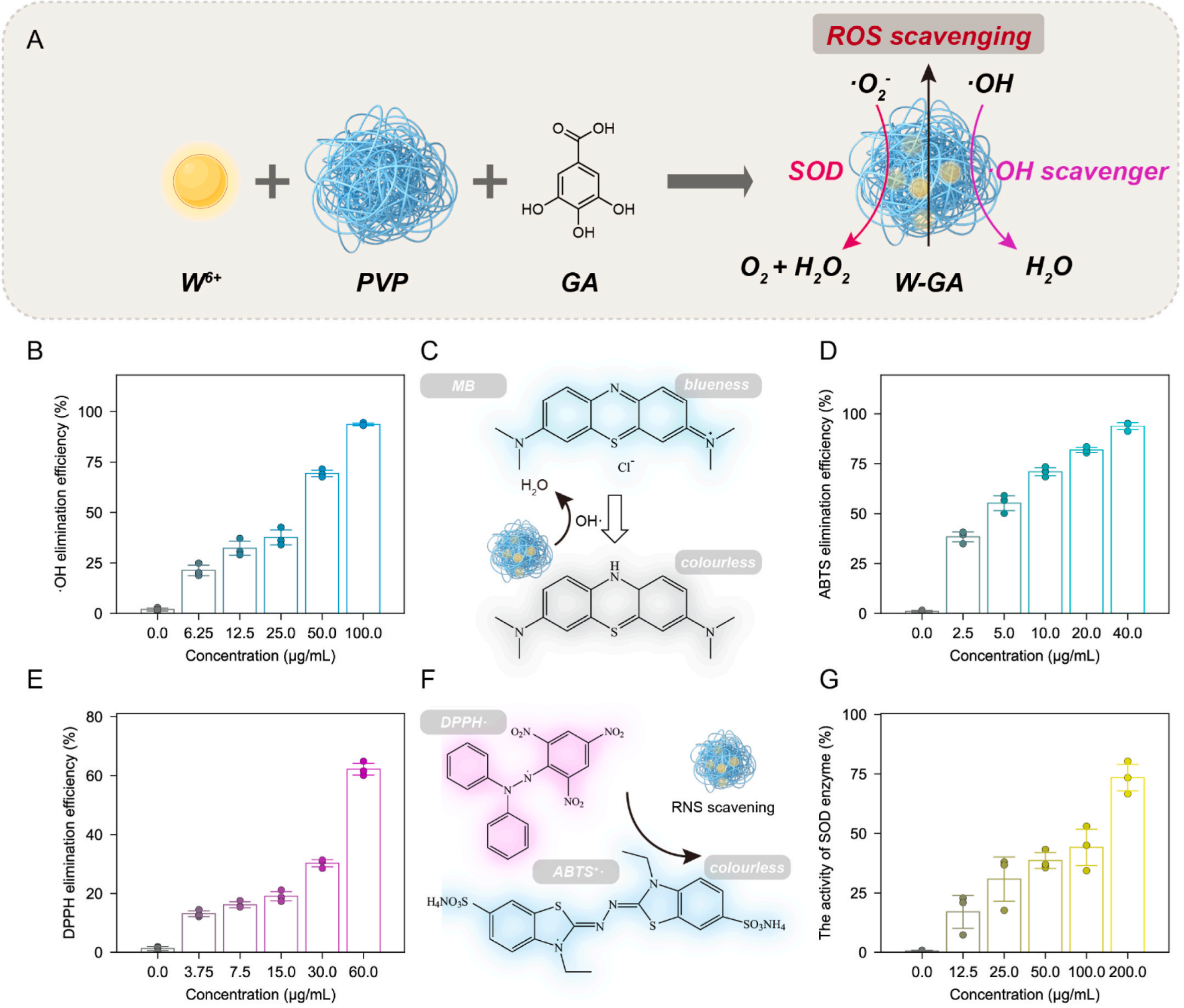

Fig. 2. In vitro evaluation of the ROS-scavenging ability of W-GA nanodots. A) A schematic representation illustrating the synthesis process of W-GA nanodots. **B)** The ability of W-GA nanodots to scavenge hydroxyl radicals was assessed via the methylene blue discoloration method (n = 3). **C)** Mechanistic diagram depicting the color change of methylene blue. **D)** The scavenging activity of nitrogen radicals was determined through ABTS assays (n = 3). **E)** Further assessment of nitrogen radical scavenging was conducted via DPPH assays (n = 3). **F)** A diagram illustrating the mechanisms of DPPH and ABTS radical scavenging. **G)** The enzyme-like activity of W-GA nanodots was evaluated via a SOD enzyme assay kit (n = 3). All the data are presented as the means ± standard deviations.

inner to the outer leaflet of the cell membrane, and Annexin V selectively binds to the exposed phosphatidylserine. Propidium iodide (PI) stains necrotic cells or cells that have lost membrane integrity during late apoptosis, resulting in red fluorescence [42]. Representative images of calcein-AM/PI staining (Fig. 3C) further confirmed the cytoprotective effects. In the control group, 88.5 % of the cells were viable, while hydrogen peroxide exposure increased the proportion of apoptotic cells to 44.9 %. Treatment with GA or W-GA nanodots reduced apoptosis to 26.9 % and 10.5 %, respectively, resulting in a marked decrease in cell death, particularly in the W-GA nanodot-treated group. To assess the impact of W-GA nanodots on cell migration, a wound healing assay was performed (Fig. 3D), which revealed enhanced cell migration in the W-GA group at 24 h posttreatment, suggesting that the nanodots promote not only survival but also wound repair mechanisms at the cellular level. Further quantification of the apoptosis rates via flow cytometry (Fig. 3E) revealed that treatment with W-GA nanodots significantly reduced apoptosis compared with treatment with hydrogen peroxide alone, supporting the observed protective effect. Confocal microscopy images of ROS levels visualized via DCFH-DA staining (Fig. 3F) confirmed these results. In the hydrogen peroxide-induced group, strong green fluorescence indicated high levels of ROS, whereas fluorescence was markedly reduced in the GA- and W-GA nanodot-treated groups, indicating effective ROS scavenging. In conclusion, these findings provide compelling evidence that W-GA nanodots not only efficiently scavenge ROS but also offer significant cytoprotection, thereby supporting their potential therapeutic application in oxidative stress-related conditions, such as impaired wound healing.

To delineate the molecular basis of oxidative stress responses in macrophages, we performed transcriptomic profiling of H_2O_2-treated RAW 264.7 cells (100 μM, 6 h) and untreated controls. Confocal imaging confirmed the efficient cellular internalization (>85 % uptake rate) of the Cy5.5-labeled W-GA nanodots (after 2 h of incubation), confirming their bioavailability for redox modulation studies (Fig. 4A, Supporting Information, Fig. S5). Differential expression analysis revealed 119

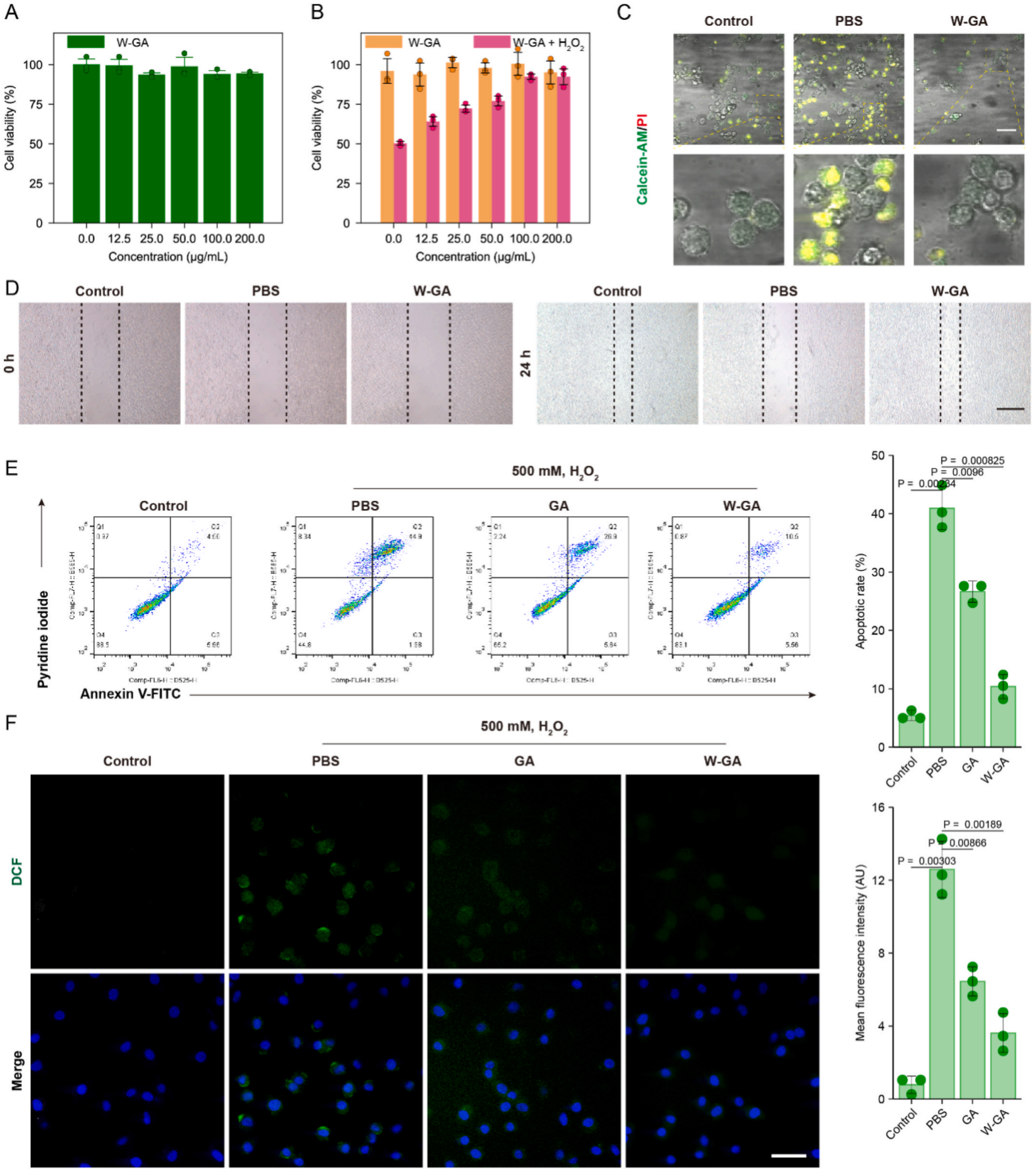

Fig. 3. W-GA nanodots demonstrate cytoprotective effects by scavenging ROS. A) Viability of cells incubated with various concentrations of W-GA nanodots for 24 h. **B)** Cell viability was assessed in the presence or absence of H_2O_2 across different concentrations of W-GA nanodots. **C)** Representative images of cells stained with calcein-AM/PI to evaluate viability in the treatment groups. **D)** Wound healing assay showing cell migration at 0 and 24 h after treatment in different groups. **E)** Apoptosis rates were quantified by flow cytometry via annexin V and propidium iodide staining, with statistical analysis on the right. **F)** Confocal microscopy images of ROS levels in various groups following DCFH-DA staining, with the corresponding fluorescence intensity quantified on the right. Scale bar, 50 μm. The data are presented as the means ± standard deviations.

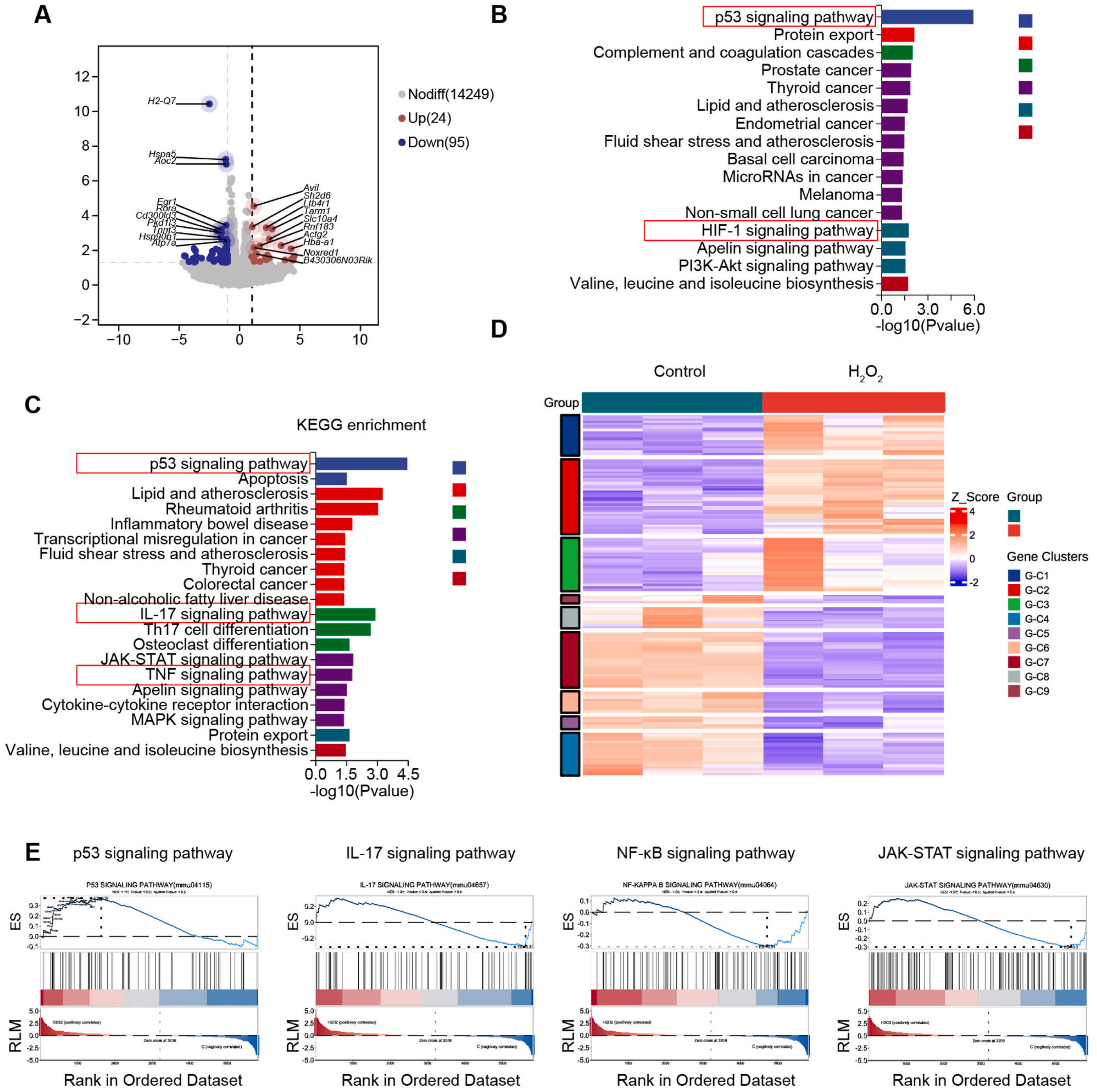

Fig. 4. Mechanistic insights into hydrogen peroxide-induced oxidative stress in macrophages. A) Volcano plot: Comparison between the H_2O_2-treated group and the control group revealed DEGs, highlighting those that were significantly upregulated and downregulated. **B)** KEGG pathway enrichment analysis: This analysis identified enriched pathways associated with upregulated genes in the H_2O_2-treated group compared with the normal control group. **C)** KEGG pathway analysis of differentially expressed genes. This analysis explored the key pathways involved in the differential gene expression observed between the two groups. **D)** Heatmap: A heatmap visualizes the gene expression differences between the control and H_2O_2-treated groups, providing an overview of the expression patterns. **E)** KEGG-GSEA: Gene set enrichment analysis (GSEA) was employed to compare pathway differences between the two groups, elucidating the functional significance of the observed changes.

significantly regulated genes (24 upregulated, 95 downregulated; $|\log2FC| > 1$, $FDR < 0.05$) from 14,322 detected transcripts, with KEGG enrichment revealing dominant pathways. Bidirectional clustering analysis further confirmed the distinct gene expression profiles between the control and H_2O_2-treated groups, highlighting the robustness of the transcriptional changes induced by oxidative stress (Supporting Information, Fig. S6). Principal component analysis (PCA) revealed clear separation between the two groups, with the first and second principal components capturing the majority of the variance, underscoring the global impact of H_2O_2 treatment on macrophage gene expression (Supporting Information, Fig. S7). To further explore the biological processes involved, we performed Kyoto Encyclopedia of Genes and Genomes (KEGG) pathway enrichment analysis on the genes whose expression was upregulated in the H_2O_2-treated group (Fig. 4B). KEGG (Kyoto Encyclopedia of Genes and Genomes) provides a comprehensive resource for mapping gene sets to known biological pathways, facilitating the understanding of cellular functions [43]. This analysis revealed significant upregulation of stress-related pathways, including the “p53 signaling pathway” and the “HIF-1 signaling pathway,” both of which are crucial for cellular responses to stress. A broader KEGG pathway analysis of all the DEGs highlighted the activation of several inflammatory pathways, including the “IL-17 signaling pathway,” “TNF signaling pathway,” and “p53 signaling pathway” (Fig. 4C). These findings suggest that the oxidative stress induced by H_2O_2 triggers the activation of key inflammatory pathways. Trend analysis of gene expression patterns within clusters revealed consistent upregulation or downregulation of genes in response to H_2O_2 treatment, with the central line representing the average expression level of all genes in each cluster (Supporting Information, Fig. S8). To provide a more comprehensive overview of the gene expression changes, a heatmap (Fig. 4D) was generated, which visually represented the differential gene expression patterns. The heatmap confirmed that H_2O_2 treatment led to distinct gene expression changes compared with those in the control group. Additionally, we conducted a KEGG-GSEA (gene set enrichment analysis) (Fig. 4E) to identify enriched pathways between the two groups. GSEA is a computational approach that evaluates whether predefined

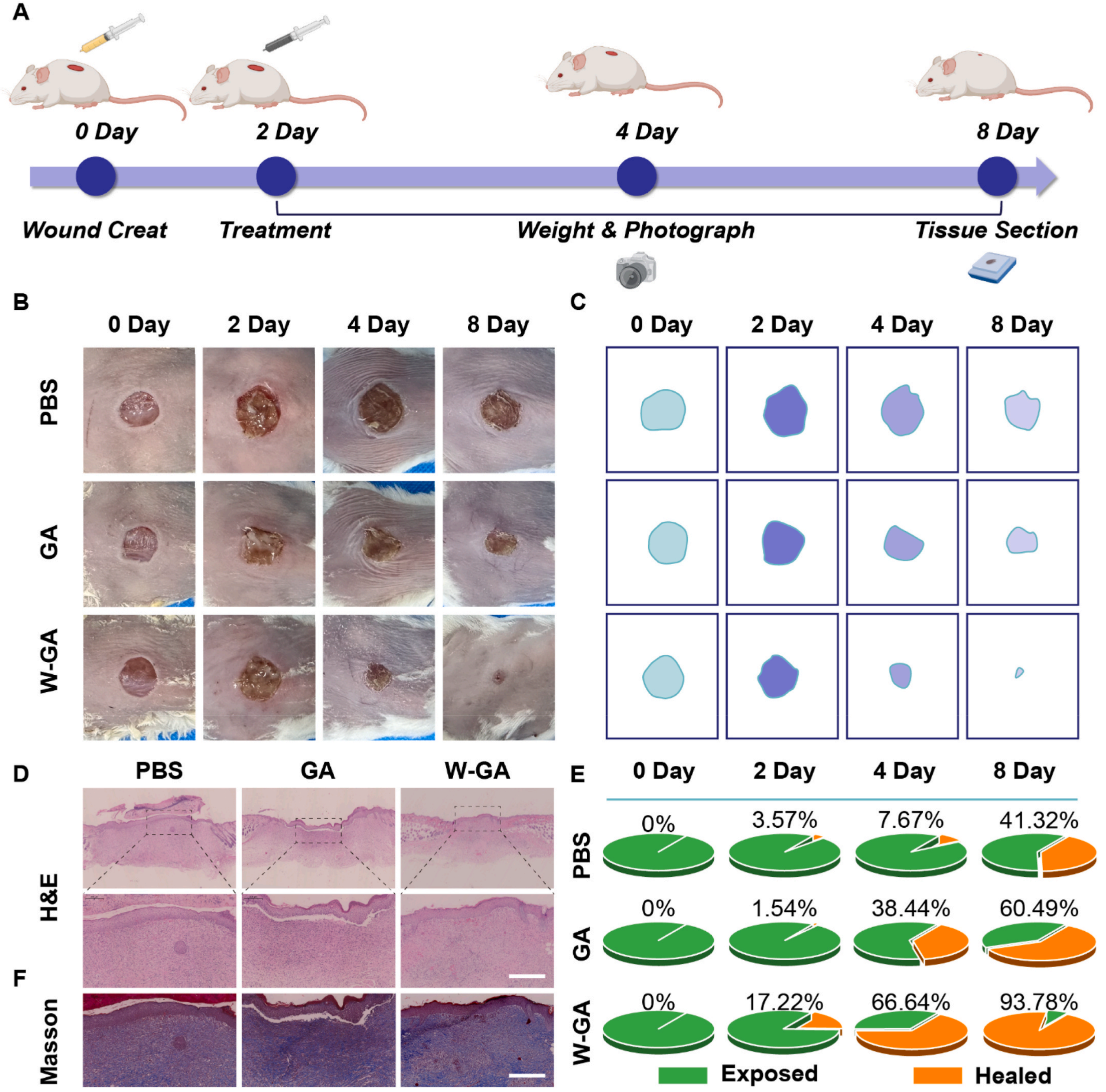

Fig. 5. Protective effects of W-GA nanodots on acute wound healing. A) Schematic diagram depicting the wound creation process and the timeline for drug administration. **B)** Representative images of wound healing in mice treated with PBS, GA, or W-GA at various time points. **C)** Quantitative analysis of wound size on the basis of images generated via Adobe Photoshop. **D)** Histological analysis of wound tissue from different treatment groups via H&E staining. Scale bar, 400 μm. **E)** Statistical analysis of wound healing percentages in each group at different time points. **F)** Masson’s Trichrome staining showing collagen deposition in the wound areas of each group. Scale bar, 400 μm.

gene sets show statistically significant differences between two biological conditions [44]. This analysis revealed enrichment of inflammatory pathways, such as the “NF-κB signaling pathway,” “IL-17 signaling pathway,” and “JAK-STAT signaling pathway,” further supporting the role of oxidative stress in driving inflammation. Genomic mapping of differentially expressed genes across chromosomes illustrated the widespread impact of H_2O_2 treatment, with upregulated and downregulated genes distributed throughout the genome (Supporting Information, Fig. S9). Protein–protein interaction (PPI) network analysis identified key hub genes and their interactions, providing insights into the molecular networks underlying the oxidative stress response (Supporting Information Figure S10). Gene Ontology (GO) enrichment analysis of the downregulated genes revealed their involvement in cellular processes such as metabolism and homeostasis, whereas the upregulated genes were enriched in inflammatory and stress response pathways (Supporting Information, Fig. S11). Notably, the heatmap showed that H_2O_2 treatment did not induce significant changes in genes associated with macrophage polarization. These findings suggest that H_2O_2 exposure does not directly alter the macrophage phenotype but rather influences oxidative stress and inflammatory pathways (Supporting Information, Fig. S12). Together, these findings indicate that H_2O_2 exposure triggers a robust inflammatory response in macrophages characterized by the activation of multiple proinflammatory pathways and widespread transcriptional reprogramming.

A comparison of gene expression between H_2O_2-treated and control macrophages revealed pronounced activation of oxidative stress and proinflammatory pathways, underscoring the pivotal role of H_2O_2-induced inflammation in macrophage responses. These findings suggest that W-GA nanodots, which modulate oxidative stress and inflammatory pathways, have significant potential as a therapeutic strategy for enhancing acute wound healing. To assess their effects on wound repair, an acute wound healing model was established in BALB/c mice. After a one-week acclimatization period, the mice were randomly divided into three groups: the PBS, GA, and W-GA groups ($n = 5$ per group). All the mice had their back fur shaved, and wounds of approximately the same size were created via surgical instruments. Two days later, the plants were treated with deionized water, GA, or W-GA nanodots. Wound images were captured at 0, 2, 4, and 8 days. At the end of the experiment (day 8), the mice were euthanized, and wound tissues were collected for further analysis (Fig. 5A). Analysis of digital photographs revealed differences in wound healing among the groups. Compared with the control group, the W-GA nanodot group presented a significant reduction in wound size (Fig. 5B, C, E). H&E staining was used to assess wound healing, revealing that the control group exhibited pronounced inflammation and limited granulation tissue formation, with a high number of inflammatory cells and low re-epithelialization. In contrast, the GA group presented reduced inflammation, increased granulation tissue, and more organized tissue structure, indicating an improvement in healing. The W-GA group demonstrated the most pronounced healing effects, with significantly reduced inflammation, abundant granulation tissue, and well-organized tissue structure, indicating that W-GA treatment accelerated wound healing (Fig. 5D). Masson staining further highlighted significant differences among the groups. The control group had minimal collagen deposition and a loose tissue structure, reflecting slower healing. The GA group presented increased collagen deposition and a more organized tissue structure, indicating that GA effectively promoted collagen formation and tissue repair. The W-GA group presented the most substantial collagen deposition and optimal tissue structure, significantly accelerating the wound healing process (Fig. 5F). Images from days 0–8 revealed slower healing in the control group, with progressively improved healing in the GA and W-GA groups, with the latter showing the most significant effect.

The therapeutic efficacy of W-GA nanoparticles in acute wound healing was validated through animal experiments. To further investigate the mechanism by which W-GA nanoparticles accelerate wound healing, we conducted transcriptomic sequencing on collected skin tissues (with three samples per group). Principal component analysis (PCA) was employed to reduce the dimensionality of the high-dimensional data to two or three dimensions while preserving the primary variance features, thereby simplifying the data complexity. PCA clusters similar samples together, with closer distances indicating greater similarity between samples. The PCA results revealed significant differences between the control group and the W-GA nanoparticle group (Fig. 6A). Differential gene expression was analyzed via DESeq with criteria set to $|\text{log2FoldChange}| > 1$ and a significance threshold of $P < 0.05$. Compared with the control group, the W-GA nanoparticle treatment group presented 200 upregulated genes and 42 downregulated genes (Fig. 6B). A bidirectional clustering analysis of the differential genes across all comparison groups was performed, clustering on the basis of gene expression levels in different samples and expression patterns of different genes within the same sample. The Euclidean distance method was used for distance calculation, and hierarchical clustering with the complete linkage method was applied. The results indicated that samples from the control group and the W-GA nanoparticle group were clustered separately (Fig. 6C). On the basis of genomic information and RNA differential expression analysis, the differentially expressed RNAs were identified in the genome (Fig. 6D). GO enrichment analysis was performed via topGO, which calculates the gene lists and counts for each GO term, and P values were computed via the hypergeometric distribution method (with significant enrichment defined as a P value < 0.05) to identify GO terms with significant enrichment of differential genes compared with the entire genomic background. The results revealed that “structural constituents of the skin epidermis,” “epidermal development,” and “epidermal cell differentiation” were significantly associated with wound healing (Fig. 6E). KEGG enrichment analysis was conducted to assess enrichment on the basis of the Rich factor, FDR value, and number of genes enriched in each pathway. The Rich factor represents the ratio of differentially expressed genes in a specific pathway to the total number of annotated differential genes, with a higher Rich factor indicating greater enrichment. The FDR value ranges from 0 to 1, with values closer to zero indicating more significant enrichment. The top 20 KEGG pathways with the smallest FDR values were selected for presentation. The results revealed that the “*Staphylococcus aureus* infection” signaling pathway was significantly associated with acute wound healing (Fig. 6F). The heatmap revealed that the expression patterns of inflammatory factors were similar between the control group and the W-GA-treated group, suggesting that W-GA nanodots may modulate inflammation rather than directly altering the expression of proinflammatory or anti-inflammatory cytokines (Supporting Information, Fig. S13). These data suggest that W-GA nanoparticles can accelerate wound healing by promoting skin cell differentiation.

4. Conclusions

In conclusion, this study presents the successful synthesis and application of W-GA nanodots as a novel therapeutic approach for chronic wound healing. By leveraging the superior ROS scavenging capabilities of W-GA nanodots, we were able to modulate the redox balance and restore immune homeostasis within the chronic wound microenvironment. The biocompatibility and antioxidant properties endowed by tungsten−gallic acid coordination significantly enhanced wound healing in chronic diabetic wound models. Our findings demonstrate the potential of W-GA nanodots to activate key wound repair pathways, promoting fibroblast-to-myofibroblast differentiation, collagen synthesis, and angiogenesis. This work not only advances the understanding of nanozyme-based therapies for chronic wounds but also offers a promising and adaptable strategy for improving patient outcomes in clinical settings. The simplicity and effectiveness of the W-GA nanodot synthesis process further underscore the potential for its widespread application in chronic wound management.

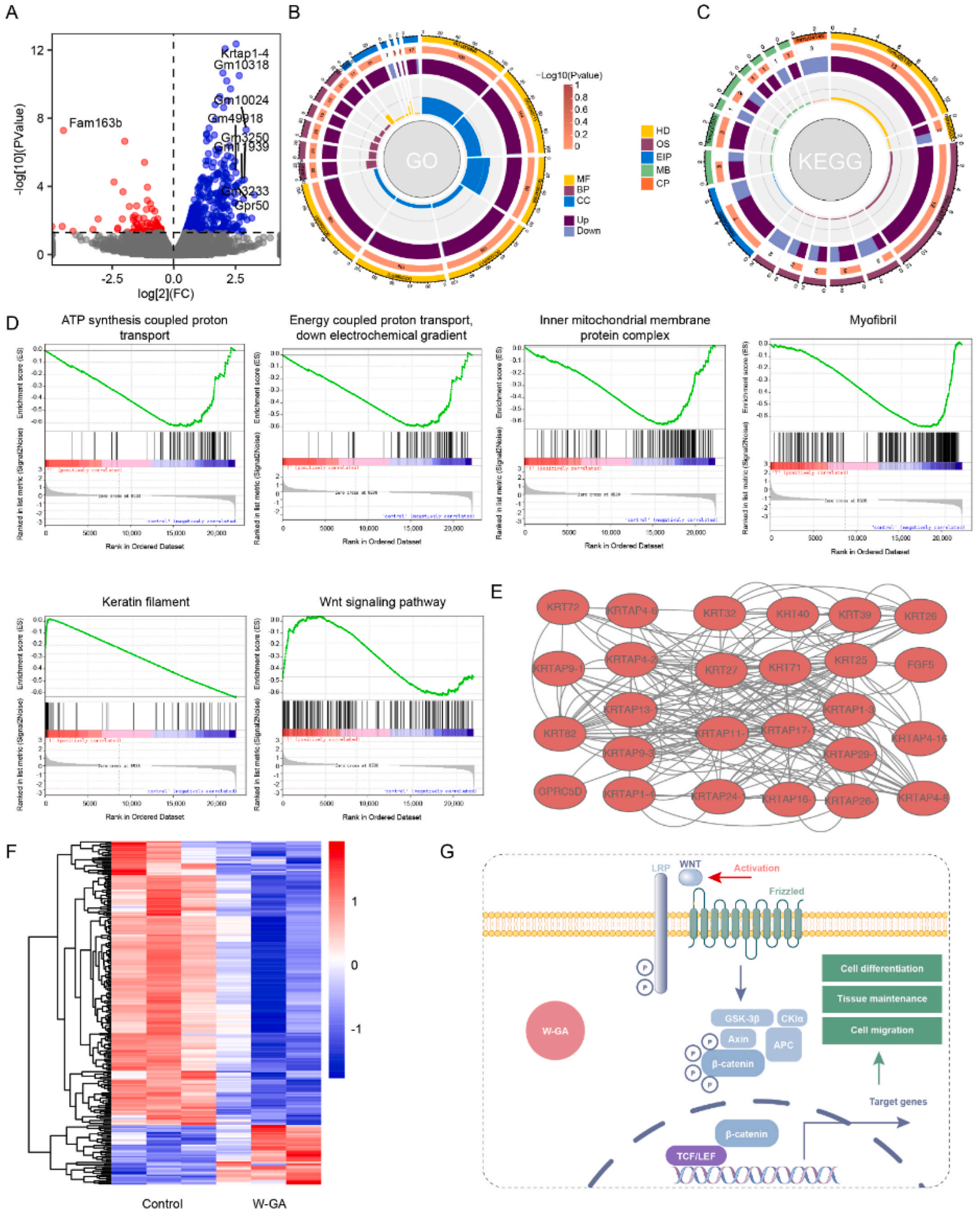

(caption on next page)

Fig. 6. Mechanisms by which W-GA nanodots confer protection against acute wounds. A) Principal component analysis (PCA) of the control and W-GA groups ($n = 3$). **B)** The distribution of genes, along with their fold-change differences and significance levels, is visualized via a volcano plot. Under normal conditions, the plot typically shows a roughly symmetrical distribution of differentially expressed genes. Genes that are downregulated in the case group compared with the control group are depicted on the left, whereas those that are upregulated are shown on the right. **C)** Clustering analysis was employed to assess the expression patterns of differentially expressed genes across various experimental conditions. **D)** Differentially expressed RNAs were mapped onto the genome on the basis of genomic information and RNA differential expression analysis results. **E)** Gene Ontology (GO) enrichment analysis of upregulated genes. The outermost ring represents the chromosomal bands, with differential expression analysis results displayed in concentric layers moving inward. The red and green bars depict the log2FoldChange values for upregulated and downregulated genes, respectively, whereas the gray dots represent the log2FoldChange values of genes without significant differential expression. **F)** Kyoto Encyclopedia of Genes and Genomes (KEGG) enrichment analysis of upregulated genes.

CRediT authorship contribution statement

Yang Zheng: Writing – original draft, Methodology, Investigation. **Qingrong Li:** Writing – original draft, Methodology, Investigation. **Xu Jin:** Writing – original draft, Methodology, Investigation. **Mengmei Zhu:** Writing – original draft, Methodology, Investigation. **Qian Liang:** Writing – original draft, Methodology, Investigation. **Yingjie Wu:** Writing – original draft, Methodology, Investigation. **Fuqiang Pan:** Writing – original draft, Methodology, Investigation. **Houhuang Qiu:** Writing – original draft, Methodology, Investigation. **Xianwen Wang:** Writing – review & editing, Supervision, Project administration, Conceptualization. **Decheng Lu:** Writing – review & editing, Supervision, Conceptualization. **Huiqiao Huang:** Writing – review & editing, Supervision, Conceptualization.

Availability of data and materials

Not applicable.

Ethics approval and consent to participate

Not applicable.

Consent for publication

Not applicable.

Funding

This work was supported by the National Natural Science Foundation of China (82372552), the Excellent Youth of Natural Science Research Projects in Anhui Province Universities, China (2023AH030060), the Basic and Clinical Cooperative Research and Promotion Program of Anhui Medical University, China (2021xkjT028), and the Research Fund of Anhui Institute of Translational Medicine, China (2022zhyx-C01).

Declaration of competing interest

The authors declare no competing financial interest.

Acknowledgments

The authors thank the Center for Scientific Research of Anhui Medical University for their valuable help with our experiments. The authors would like to thank the Shiyanjia laboratory (www.shiyanjia.com) for the XPS test.

Appendix A. Supplementary data

Supplementary data to this article can be found online at https://doi.org/10.1016/j.mtbio.2025.101662.

Data availability

Data will be made available on request.

References

[1] G.C. Gurtner, S. Werner, Y. Barrandon, M.T. Longaker, Wound repair and regeneration, Nature 453 (7193) (2008) 314–321.

[2] D.G. Armstrong, G.C. Gurtner, A histologically hostile environment made more hospitable? Nat. Rev. Endocrinol. 14 (9) (2018) 511–512.

[3] J.G. Powers, C. Higham, K. Broussard, T.J. Phillips, Wound healing and treating wounds: chronic wound care and management, J. Am. Acad. Dermatol. 74 (4) (2016) 607–625.

[4] S.A. Eming, P. Martin, M. Tomic-Canic, Wound repair and regeneration: mechanisms, signaling, and translation, Sci. Transl. Med. 6 (265) (2014), 265sr6-265sr6.

[5] Y. Zhang, S. Wang, Y. Yang, S. Zhao, J. You, J. Wang, J. Cai, H. Wang, J. Wang, W. Zhang, J. Yu, C. Han, Y. Zhang, Z. Gu, Scarless wound healing programmed by core-shell microneedles, Nat. Commun. 14 (1) (2023) 3431.

[6] R. Ankawa, Y. Fuchs, More than one way to skin a wound, Cell Stem Cell 23 (5) (2018) 636–638.

[7] A. Veves, V. Falanga, D.G. Armstrong, M.L. Sabolinski, S. the, Apligraf diabetic foot ulcer, graftskin, a human skin equivalent, is effective in the management of noninfected neuropathic diabetic foot ulcers: a prospective randomized multicenter clinical trial, Diabetes Care 24 (2) (2001) 290–295.

[8] W.A. Marston, J. Hanft, P. Norwood, R. Pollak, G. for the dermagraft diabetic foot ulcer study, the efficacy and safety of dermagraft in improving the healing of chronic diabetic foot ulcers: results of a prospective randomized trial, Diabetes Care 26 (6) (2003) 1701–1705.

[9] M. Cruciani, B.A. Lipsky, C. Mengoli, F. de Lalla, Are Granulocyte colony–stimulating factors beneficial in treating diabetic foot infections?: a meta-analysis, Diabetes Care 28 (2) (2005) 454–460.

[10] M. Rodrigues, N. Kosaric, C.A. Bonham, G.C. Gurtner, Wound healing: a cellular perspective, Physiol. Rev. 99 (1) (2019) 665–706.

[11] Y. Zhang, G. Wei, W. Liu, T. Li, Y. Wang, M. Zhou, Y. Liu, X. Wang, H. Wei, Nanozymes for nanohealthcare, Nat. Rev. Methods. Primers. 4 (1) (2024) 36.

[12] R. Zhang, K. Fan, X. Yan, Nanozymes: created by learning from nature, Science China, Life Sci. 63 (8) (2020) 1183–1200.

[13] X. Mou, Q. Wu, Z. Zhang, Y. Liu, J. Zhang, C. Zhang, X. Chen, K. Fan, H. Liu, Nanozymes for regenerative medicine, Small Methods 6 (11) (2022) e2200997.

[14] Y. Huang, J. Ren, X. Qu, Nanozymes: classification, catalytic mechanisms, activity regulation, and applications, Chem. Rev. 119 (6) (2019) 4357–4412.

[15] J. Li, S. Song, J. Meng, L. Tan, X. Liu, Y. Zheng, Z. Li, K.W.K. Yeung, Z. Cui, Y. Liang, S. Zhu, X. Zhang, S. Wu, 2D MOF periodontitis photodynamic ion therapy, J. Am. Chem. Soc. 143 (37) (2021) 15427–15439.

[16] X. Ji, L. Ge, C. Liu, Z. Tang, Y. Xiao, W. Chen, Z. Lei, W. Gao, S. Blake, D. De, B. Shi, X. Zeng, N. Kong, X. Zhang, W. Tao, Capturing functional two-dimensional nanosheets from sandwich-structure vermiculite for cancer theranostics, Nat. Commun. 12 (1) (2021) 1124.

[17] Y. Zhao, S. Song, D. Wang, H. Liu, J. Zhang, Z. Li, J. Wang, X. Ren, Y. Zhao, Nanozyme-reinforced hydrogel as a H2O2-driven oxygenerator for enhancing prosthetic interface osseointegration in rheumatoid arthritis therapy, Nat. Commun. 13 (1) (2022) 6758.

[18] R. Hou, T. Lu, W. Gao, J. Shen, Z. Yu, D. Li, R. Zhang, Y. Zheng, X. Cai, Prussian blue nanozyme promotes the survival rate of skin flaps by maintaining a normal microenvironment, ACS Nano 16 (6) (2022) 9559–9571.

[19] G. Zhang, D. Song, R. Ma, M. Li, B. Liu, Z. He, Q. Fu, Artificial mucus layer formed in response to ROS for the oral treatment of inflammatory bowel disease, Sci. Adv. 10(30) eado8222.

[20] T. Wei, T. Pan, X. Peng, M. Zhang, R. Guo, Y. Guo, X. Mei, Y. Zhang, J. Qi, F. Dong, M. Han, F. Kong, L. Zou, D. Li, D. Zhi, W. Wu, D. Kong, S. Zhang, C. Zhang, Janus liposozyme for the modulation of redox and immune homeostasis in infected diabetic wounds, Nat. Nanotechnol. 19 (8) (2024) 1178–1189.

[21] Y. Xie, W. Hou, X. Song, Y. Yu, J. Huang, X. Sun, R. Kang, D. Tang, Ferroptosis: process and function, Cell Death Differ. 23 (3) (2016) 369–379.

[22] Q. Pan, L. Xie, H. Zhu, Z. Zong, D. Wu, R. Liu, B. He, Y. Pu, Curcumin-incorporated EGCG-based nano-antioxidants alleviate colon and kidney inflammation via antioxidant and anti-inflammatory therapy, Regen Biomater. 11 (2024) rbae122.

[23] Q. Pan, L. Xie, P. Cai, D. Wu, H. Zhu, L. Xu, R. Liu, K. Luo, B. He, Y. Pu, Acid-resistant nano-antioxidants based on Epigallocatechin gallate alleviate acute intestinal and kidney inflammation, ACS Appl. Mater. Interfaces 16 (35) (2024) 46090–46101.

[24] W. Wang, Y. Gao, W. Xu, Y. Xu, N. Zhou, Y. Li, M. Zhang, B.Z. Tang, The one-stop integrated nanoagent based on photothermal therapy for deep infection healing and inflammation inhibition, Adv. Mater. 36 (3) (2024) e2307785.

[25] Q. Li, C. Zhang, M. Zhu, J. Shan, H. Qian, Y. Ma, X. Wang, W-GA nanodots restore intestinal barrier functions by regulating flora disturbance and relieving excessive oxidative stress to alleviate colitis, Acta Biomater. 182 (2024) 260–274.

[26] R. Ruszat, S. Wyler, T. Forster, O. Reich, C.G. Stief, T.C. Gasser, T. Sulser, A. Bachmann, Safety and effectiveness of photoselective vaporization of the prostate (PVP) in patients on ongoing oral Anticoagulation, Eur. Urol. 51 (4) (2007) 1031–1041.

[27] J. Du, Z. Gu, L. Yan, Y. Yong, X. Yi, X. Zhang, J. Liu, R. Wu, C. Ge, C. Chen, Y. Zhao, Poly(Vinylpyrollidone)- and selenocysteine-modified Bi(2) Se(3) nanoparticles enhance radiotherapy efficacy in tumors and promote radioprotection in normal tissues, Adv. Mater. 29 (34) (2017).

[28] I. Zarandona, A.I. Puertas, M.T. Dueñas, P. Guerrero, K. de la Caba, Assessment of active chitosan films incorporated with gallic acid, Food Hydrocoll. 101 (2020) 105486.

[29] S. Shen, D. Jiang, L. Cheng, Y. Chao, K. Nie, Z. Dong, C.J. Kutyreff, J.W. Engle, P. Huang, W. Cai, Z. Liu, Renal-clearable ultrasmall coordination polymer nanodots for chelator-free (64)Cu-labeling and imaging-guided enhanced radiotherapy of cancer, ACS Nano 11 (9) (2017) 9103–9111.

[30] Z. Xu, B. Lu, Q. Xiang, Y. Li, S. Li, Y. Lin, J. Pang, Radical-scavenging activities of marine-derived xyloketals and related chromanes, Acta Pharm. Sin. B 3 (5) (2013) 322–327.

[31] M. Elbaum, Quantitative cryo-scanning transmission electron microscopy of biological materials, Adv. Mater. 30 (41) (2018) e1706681.

[32] J.J.P. Peters, B.W. Reed, Y. Jimbo, K. Noguchi, K.H. Müller, A. Porter, D.J. Masiel, L. Jones, Event-responsive scanning transmission electron microscopy, Science 385 (6708) (2024) 549–553.

[33] D. Grasseschi, W.C. Silva, R.d. Souza Paiva, L.D. Starke, A.S. do Nascimento, Surface coordination chemistry of graphene: understanding the coordination of single transition metal atoms, Coord. Chem. Rev. 422 (2020) 213469.

[34] J. Gupta, Hexaco-ordination of Tellurium, Molybdenum and tungsten, Nature 140 (3546) (1937) 685, 685.

[35] H. Sies, V.V. Belousov, N.S. Chandel, M.J. Davies, D.P. Jones, G.E. Mann, M. P. Murphy, M. Yamamoto, C. Winterbourn, Defining roles of specific reactive oxygen species (ROS) in cell biology and physiology, Nat. Rev. Mol. Cell Biol. 23 (7) (2022) 499–515.

[36] P. Strzyz, ATP and ROS signal cell extrusion, Nat. Rev. Mol. Cell Biol. 23 (6) (2022) 387, 387.

[37] Z. Liu, T.S. Xiao, Partners with a killer: Metabolic signaling promotes inflammatory cell death, Cell 184 (17) (2021) 4374–4376.

[38] H. Xing, Z. Zhang, Y. Song, g. shi, E. Harrington, J. Feng, Abstract 15033: chronic inhibition of Mitochondrial reactive oxygen species protects against Endothelial SK channel Dysfunction in diabetes, Circulation 142 (Suppl_3) (2020) A15033. A15033.

[39] R. Liebers, D. Jäger, Surgical wound immunotherapy, Nat. Nanotechnol. 14 (1) (2019) 7–8.

[40] Z. Ge, W. Guo, Y. Tao, H. Sun, X. Meng, L. Cao, S. Zhang, W. Liu, M.L. Akhtar, Y. Li, Y. Ren, Wireless and closed-loop smart dressing for Exudate management and on-demand treatment of chronic wounds, Adv. Mater. 35 (47) (2023) e2304005.

[41] Z. Wang, R. Zhang, X. Yan, K. Fan, Structure and activity of nanozymes: Inspirations for de novo design of nanozymes, Mater. Today 41 (2020) 81–119.

[42] V. Sisirak, B. Sally, V. D'Agati, W. Martinez-Ortiz, Z.B. Özçakar, J. David, A. Rashidfarrokhi, A. Yeste, C. Panea, A.S. Chida, M. Bogunovic, I.I. Ivanov, F. J. Quintana, I. Sanz, K.B. Elkon, M. Tekin, F. Yalçınkaya, T.J. Cardozo, R. M. Clancy, J.P. Buyon, B. Reizis, Digestion of chromatin in apoptotic cell Microparticles prevents Autoimmunity, Cell 166 (1) (2016) 88–101.

[43] M. Kanehisa, S. Goto, KEGG: kyoto encyclopedia of genes and genomes, Nucleic Acids Res. 28 (1) (2000) 27–30.

[44] A. Subramanian, P. Tamayo, V.K. Mootha, S. Mukherjee, B.L. Ebert, M.A. Gillette, A. Paulovich, S.L. Pomeroy, T.R. Golub, E.S. Lander, J.P. Mesirov, Gene set enrichment analysis: a knowledge-based approach for interpreting genome-wide expression profiles, Proc. Natl. Acad. Sci. U. S. A 102 (43) (2005) 15545–15550.